

Palaeoarchaean deep mantle heterogeneity recorded by enriched plume remnants

Chao Wang^{1,2*}, Shuguang Song^{1*}, Chunjing Wei¹, Li Su³, Mark B. Allen⁴, Yaoling Niu^{2,4}, Xian-Hua Li⁵ and Jinlong Dong¹

The thermal and chemical state of the early Archaean deep mantle is poorly resolved due to the rare occurrences of early Archaean magnesium-rich volcanic rocks. In particular, it is not clear whether compositional heterogeneity existed in the early Archaean deep mantle and, if it did, how deep mantle heterogeneity formed. Here we present a geochronological and geochemical study on a Palaeoarchaean ultramafic-mafic suite (3.45-Gyr-old) with mantle plume signatures in Longwan, Eastern Hebei, the North China Craton. This suite consists of metamorphosed cumulates and basalts. The meta-basalts are iron rich and show the geochemical characteristics of present-day oceanic island basalt and unusually high mantle potential temperatures (1,675 °C), which suggests a deep mantle source enriched in iron and incompatible elements. The Longwan ultramafic-mafic suite is best interpreted as the remnants of a 3.45-Gyr-old enriched mantle plume. The first emergence of mantle-plume-related rocks on the Earth 3.5–3.45 billion years ago indicates that a global mantle plume event occurred with the onset of large-scale deep mantle convection in the Palaeoarchaean. Various deep mantle sources of these Palaeoarchaean mantle-plume-related rocks imply that significant compositional heterogeneity was present in the Palaeoarchaean deep mantle, most probably introduced by recycled crustal material.

Magnesium-rich lavas (for example, komatiites and picrites) are rare in Earth history, and are typically produced by adiabatic decompression melting of upwelling mantle plumes that are significantly hotter than the ambient mantle^{1–3}. The close affinity of komatiites and picrites with their primary magmas means that they can probe the thermal and chemical state of the Earth's thermal boundary layer from which mantle plumes originate through time^{4–6}. Ultramafic rocks occur in the 3.8-Gyr-old greenstone belts of the North Atlantic Craton, but accumulated evidence indicates that these rocks were not mantle plume related^{7–9}. Definite records of mantle plume activities began to emerge ~3.5 billion years ago (Ga)^{1,2}, and included 3.5–3.46-Gyr-old komatiites in Barberton and East Pilbara. The geochemistry of the Archaean komatiites suggests that their deep mantle source was hot, and depleted or similar to primitive mantle, whereas the geochemistry of post-Archaean komatiites indicates a colder and heterogeneous deep mantle reservoir with enriched components introduced by the Earth's convection^{4,5}. There are no records of enriched ultramafic rocks from the Palaeoarchaean era (3.6–3.2 Ga) comparable to the picrites associated with Phanerozoic mantle plumes, but given the fragmentary nature of the geological record, it is not clear whether this reflects a genuine lack of deep mantle heterogeneity and deep mantle convection in the Palaeoarchaean or a sampling bias.

Here we report the discovery of a suite of Palaeoarchaean ultramafic-mafic rocks with a lithological assemblage of metamorphosed lherzolite, websterite, ferropicrite and ferrobasalt in the North China Craton (NCC). Geochronological and geochemical evidence indicates that these ultramafic-mafic rocks are remnants of a 3.45-Gyr-old enriched mantle plume. Based on these findings, we support the idea that a global mantle plume event occurred in

the Palaeoarchaean as a result of large-scale deep mantle convection, and significant compositional heterogeneity was present in the Palaeoarchaean deep mantle^{1,2,4}.

The Longwan ultramafic-mafic suite

The NCC is a rare craton in that it preserves ≥ 3.8 -Gyr-old crustal record, both from extant orthogneisses and from detrital zircons in younger metasedimentary rocks¹⁰. There was widespread Neoproterozoic granulite-facies metamorphism and granitic magmatism as the result of microcontinental collision^{11–13}. No Eoarchaean–Palaeoarchaean mantle-derived ultramafic-mafic rocks, especially mantle-plume-related ultramafic-mafic rocks from the NCC were reported previously. The studied ultramafic-mafic rocks were collected from the Longwan iron-mining area of Eastern Hebei in the Eastern Block of the NCC (Fig. 1a). The Longwan ultramafic-mafic suite, together with banded (or massive) iron quartzite and garnet-mica schist, occurs as hundreds of metre-to-kilometre-scaled tectonic slivers within Neoproterozoic tonalite-trondhjemite-granodiorite (TTG) gneisses (Fig. 1b). The iron quartzite lenses have been mined, and the ultramafic-mafic rocks crop out as dark-coloured wall rocks of the mining pits. Two major types of ultramafic-mafic rocks were identified based on their mineral assemblages: (1) meta-cumulates and (2) meta-basalts. They were all metamorphosed and completely recrystallized under high-pressure granulite-facies metamorphism at the end of the Neoproterozoic era and no primary igneous textures remain. The meta-cumulates occur as lens-shaped blocks and are meta-lherzolite and meta-websterite in composition (Supplementary Fig. 1a–c), and strongly recrystallized samples developed an idioblastic texture with triple junction grain boundaries close to 120° (Supplementary Fig. 2a,b). Meta-lherzolite is a

¹MOE Key Laboratory of Orogenic Belts and Crustal Evolution, School of Earth and Space Sciences, Peking University, Beijing, China. ²School of Earth Sciences and Resources, China University of Geosciences, Beijing, China. ³School of Scientific Research and State Key Laboratory of Geological Processes and Mineral Resources, China University of Geosciences, Beijing, China. ⁴Department of Earth Sciences, Durham University, Durham, UK. ⁵State Key Laboratory of Lithospheric Evolution, Institute of Geology and Geophysics, Chinese Academy of Sciences, Beijing, China. *e-mail: chao.wang@cugb.edu.cn; sgsong@pku.edu.cn

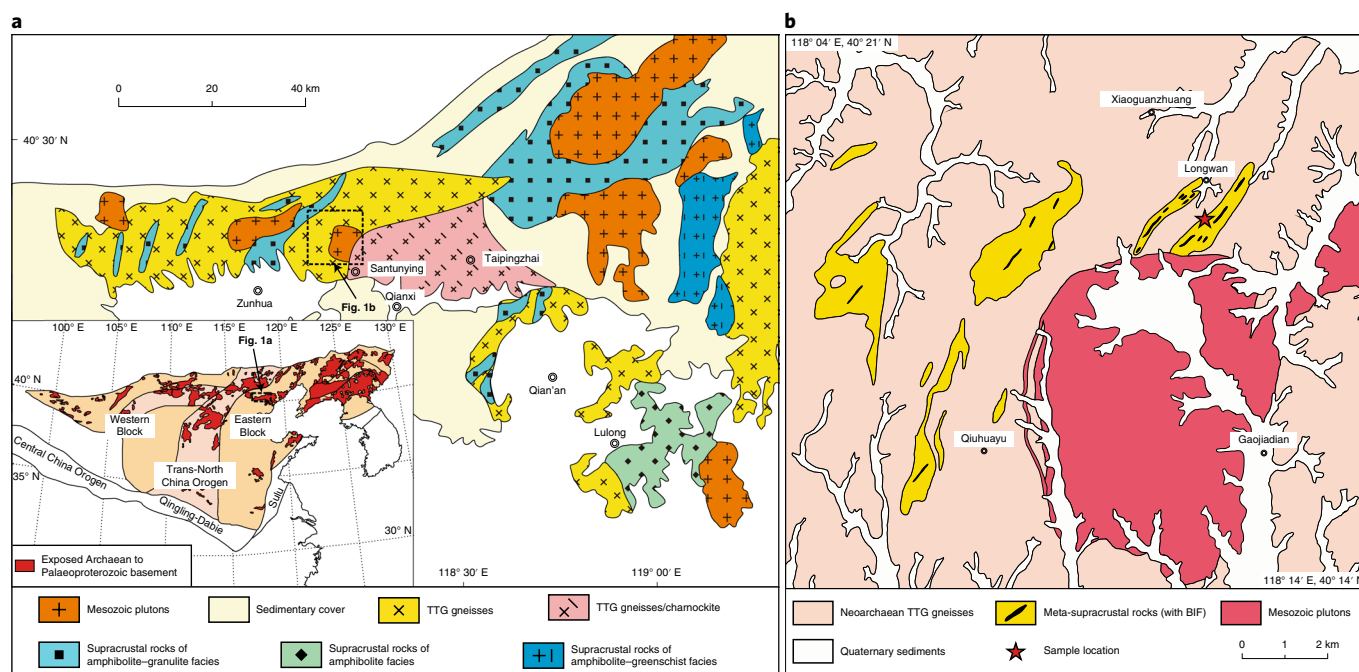


Fig. 1 | Geological maps of Eastern Hebei, the NCC and the study area. a, Inset is a sketch map of the NCC showing its major tectonic units. Eastern Hebei lies in the Eastern Block of the NCC and its Precambrian basement rocks consist of Neoproterozoic TTG gneisses, charnockites and supracrustal rocks with some Palaeo-Mesoarchaeoan supracrustal remnants and Palaeoproterozoic mafic dykes. **b**, The studied meta-cumulate and meta-basalt samples were collected from meta-supracrustal lenses from the Longwan iron-mining area of Eastern Hebei, which are within the Neoproterozoic TTG gneisses and intruded by Mesozoic plutons. BIF, banded iron formation.

rare component in the meta-cumulates and has a mineral assemblage of olivine, clinopyroxene, orthopyroxene, minor Al-rich spinel and opaque oxides (Supplementary Fig. 2a). The meta-websterite consists of clinopyroxene, orthopyroxene and amphibole, with accessory pyrite between them (Supplementary Fig. 2b). The meta-basalts are dark-green to green-coloured massive outcrops (Supplementary Fig. 1d,e) and mafic in composition. They were metamorphosed into two-pyroxene granulites (clinopyroxene, orthopyroxene, plagioclase, quartz and opaque oxides) or garnet-clinopyroxene granulites (garnet, clinopyroxene, plagioclase, quartz and opaque oxides) (Supplementary Fig. 2c,d) with very weak or no foliation. All the zircon grains from the meta-basalts are metamorphic without any magmatic cores, which gives metamorphic ages of ~ 2.5 Ga as a result of intensive Neoproterozoic tectonothermal events (our unpublished data).

In total, 125 zircon grains were extracted from a meta-websterite sample J14-46c (~ 30 kg) of the Longwan ultramafic–mafic suite. Zircons are mostly subhedral crystals, 50–100 μm in length, and show clear core–rim textures; bright cores with weakly oscillatory zoning are surrounded by dark rims in cathodoluminescence (CL) images (Fig. 2a), indicative of a metamorphic overgrowth around magmatic cores¹⁴. There are apatite inclusions in the magmatic cores, but no felsic mineral inclusions were identified within them (Supplementary Fig. 3). We analysed 28 magmatic cores and 17 metamorphic rims, and the U–Pb data are listed in Supplementary Table 1. Most analyses are discordant owing to more than one episode of radiogenic lead loss and plot under the concordia curve (Fig. 2b). A ^{207}Pb – ^{206}Pb age range of $3,475 \pm 14$ to $3,302 \pm 2$ Ma (1σ) was yielded from 28 magmatic cores with Th/U ratios generally over 0.2. They lie along a discordant line that intersects the concordia at $3,456 \pm 15$ Ma with a mean square weighted deviation (MSWD) of 1.9 (Fig. 2b), which is in accordance with the concordia age ($3,451 \pm 3$ Ma, MSWD = 0.36) and weighted mean ^{207}Pb – ^{206}Pb

age ($3,454 \pm 4$ Ma, MSWD = 8.1) of 13 analyses indistinguishable from the concordia curve (Fig. 2c). Most of the concordant analyses have Th/U ratios above 1, which is a common feature of zircons from mafic magma¹⁵. ^{207}Pb – ^{206}Pb ages that ranged from $3,279 \pm 4$ to $2,993 \pm 22$ Ma were given by 17 metamorphic rims with Th/U ratios mostly below 0.1. They define a discordant line that intercepts the concordia at $3,267 \pm 20$ Ma (MSWD = 3.9), with three concordant ^{207}Pb – ^{206}Pb ages of $3,271 \pm 1$ to $3,238 \pm 2$ Ma. Nine concordant magmatic cores were chosen for in situ trace element analyses, and the data are listed in Supplementary Table 2. Their trace element ratios are typical of zircons from mantle-derived magma, and resemble zircons from plume-influenced settings (Supplementary Fig. 4). Of the concordant to near-concordant magmatic cores (discordance $< 10\%$) from the meta-websterite sample J14-46c, 13 were selected for in situ Hf–O isotope analyses (data listed in Supplementary Table 3). These magmatic cores have initial $^{176}\text{Hf}/^{177}\text{Hf}$ ratios of 0.280569 – 0.280720 (calculated at the concordia age of $3,451 \pm 3$ Ma) with $\epsilon_{\text{Hf}}(t)$ values of 0.2–5.6, and have mantle-like $\delta^{18}\text{O}$ values from 4.10‰ to 5.58‰ (Fig. 2d).

Bulk-rock major and trace element data of the studied samples are listed in Supplementary Table 4. Samples of the Longwan ultramafic–mafic suite have systematic compositional variation, as shown in MgO variation diagrams (Supplementary Fig. 5). The meta-lherzolite samples have low contents of SiO_2 (39.84–44.86 wt%) and Al_2O_3 (3.80–5.44 wt%), but high MgO (27.76–33.03 wt%) and Mg# (84.1–85.3) (Methods) (Fig. 3b). They are slightly enriched in light rare earth elements (LREEs) over heavy rare earth elements (HREEs) with a $(\text{La}/\text{Yb})_{\text{N}}$ (N, chondrite normalized) that ranges from 2.7 to 4.7 (Fig. 3d). These meta-lherzolites have high abundances of compatible elements, such as Cr and Ni. The meta-websterites are characterized by high contents of SiO_2 (51.15–54.18 wt%) and MgO (23.28–26.55 wt%) with an accordingly high Mg# (85.5–86.8) (Fig. 3b), and compatible elements (for example, Cr and Ni). They

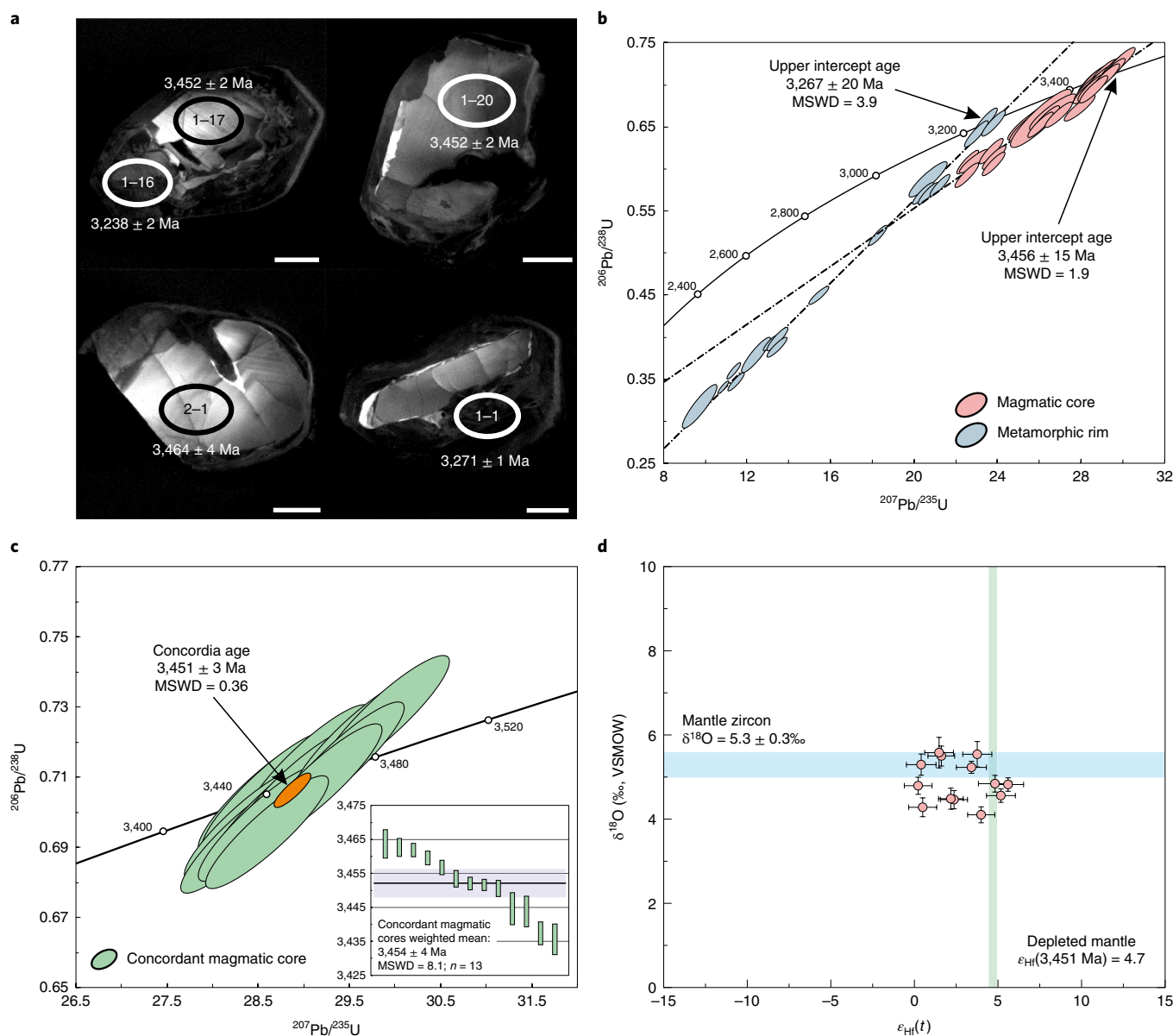


Fig. 2 | CL images, U-Pb concordia diagrams and Hf-O isotopes for zircons from the meta-websterite sample J14-46c of the Palaeoarchaean Longwan ultramafic-mafic suite. **a**, CL images of representative zircons from the meta-websterite sample J14-46c. The ellipses are in situ secondary ion mass spectrometry (SIMS) zircon U-Pb analytical spots and numbers in the ellipses are sequential numbers of analytical spots. The ages next to ellipses are zircon ^{207}Pb - ^{206}Pb ages. Scale bars, 20 μm . **b**, U-Pb concordia diagram for all the zircons from the meta-websterite sample J14-46c. **c**, U-Pb concordia diagram for concordant magmatic zircon cores from the meta-websterite sample J14-46c. Inset, the weighted mean ^{207}Pb - ^{206}Pb age of concordant magmatic zircon cores. Box heights are 1σ . **b, c**, Data-point error ellipses are 68.3% confidence. **d**, $\epsilon_{\text{Hf}}(t)$ - $\delta^{18}\text{O}$ diagram for magmatic zircon cores with discordance <10% from the meta-websterite sample J14-46c (error bars are 2σ); mantle zircon $\delta^{18}\text{O}$ values are from Valley³⁸. VSMOW, Vienna Standard Mean Ocean Water.

are relatively low in TiO_2 (0.13–0.16 wt%), Al_2O_3 (3.56–4.08 wt%) and total Fe_2O_3 ($\text{Fe}_2\text{O}_{3\text{T}}$) (8.30–8.91 wt%). They have similar trace element patterns compared with the meta-lherzolites (Fig. 3d). They show relative depletion of high field strength elements (for example, Nb, Ta, Zr and Hf) (Fig. 3d). All the meta-basalts are iron rich with $\text{Fe}_2\text{O}_{3\text{T}}$ mostly >14 wt% and variable MgO contents (7.29–19.36 wt%), and plot in the ‘alkali basalt’ field (Fig. 3a). According to their MgO contents, they can be further subdivided into meta-ferropicrites (MgO > 12 wt%) and meta-ferrobasalts (MgO < 12 wt%). The meta-ferropicrites have high contents of TiO_2 (1.61–2.10 wt%), MgO (12.57–19.36 wt%), Cr (1,162–1,494 ppm) and Ni (411–943 ppm) with SiO_2 of 43.73–49.78 wt% and Mg# of 62.1–71.9 (Fig. 3b).

They are relatively enriched in $\text{Fe}_2\text{O}_{3\text{T}}$ (15.24–16.89 wt%) (Fig. 3c) but low in Al_2O_3 (4.65–7.85 wt%). Their rare earth element (REE) abundances are much higher than those of meta-cumulates, and they also show enrichment of LREEs over HREEs ($(\text{La}/\text{Yb})_{\text{N}} = 6.7$ –8.6), which ranges between those of the enriched mid-ocean ridge basalt (MORB) and the ocean island basalt (OIB), but with a closer affinity with the OIB (Fig. 3d). They are depleted in Y and some high field strength elements (for example, Zr and Hf), but have positive anomalies of Nb and Ta. The meta-ferrobasalts have similar geochemical features to those of the meta-ferropicrites, except that they have a lower MgO (7.29–9.36 wt%) and $\text{Fe}_2\text{O}_{3\text{T}}$ (11.19–15.68 wt%) with a Mg# of 50.6–62.0 and a relatively high Al_2O_3 (6.80–11.05 wt%) and

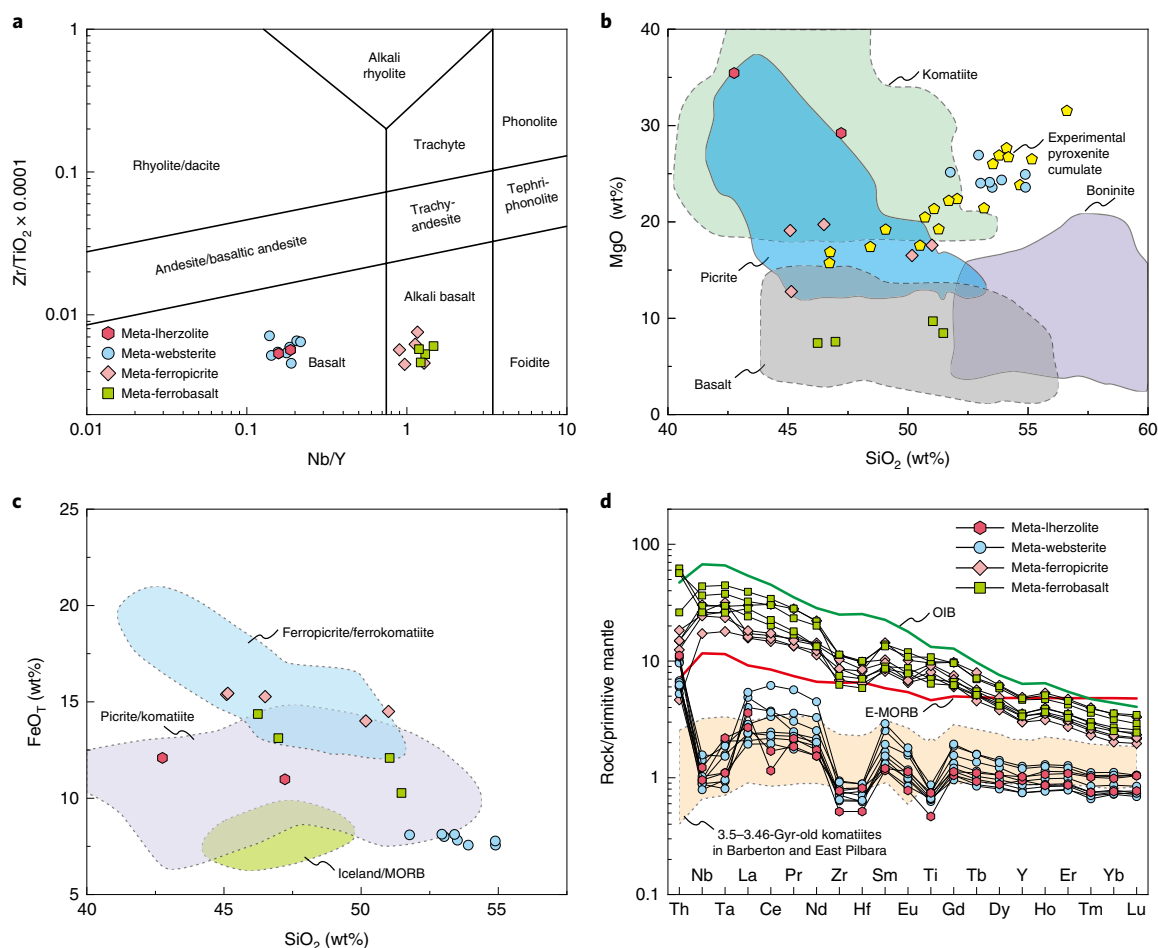


Fig. 3 | Geochemical diagrams for the Palaeoarchaean Longwan ultramafic–mafic suite. **a**, Rock classification diagram³⁹ for meta-basalts with meta-cumululates plotted for comparison. **b**, SiO_2 –MgO diagram. The fields of komatiites, picrites, basalts and boninites are constructed using the data from the GEOROC database with experimentally produced pyroxenite cumulates¹⁶ plotted for comparison. **c**, SiO_2 – FeO_T diagram. The fields of ferropicrite/ferrokomaite, picrite/komatiite and Iceland/MORB are from Gibson²⁴. Major element oxides in **a**, **b** and **c** are recalculated on an anhydrous basis. **d**, Primitive mantle-normalized trace element diagram; the values of primitive mantle, OIB and enriched MORB (E-MORB) are from Sun and McDonough⁴⁰, and the values of 3.5–3.46-Gyr-old komatiites in Barberton and East Pilbara are from Sossi et al.³. Only fluid immobile elements are plotted because they should not have been affected during high-grade metamorphism and can be used for petrogenetic interpretations.

CaO (14.36–18.05 wt%). They also have relatively high abundances of Cr (825–1,394 ppm) and Ni (499–839 ppm).

Remnants of Palaeoarchaean plume magmatism

The absence of felsic mineral inclusions (Supplementary Fig. 3) and the sharp contrast of age population, Th/U ratios and $\varepsilon_{\text{Hf}}(t)$ values between the magmatic zircon cores from the meta-websterite sample J14-46c and pre-2.8 Ga detrital or xenocrystic zircons from Eastern Hebei (Supplementary Figs. 6 and 7) argue against a xenocrystic origin of these zircons. Instead, morphological characteristics in the CL images, high Th/U ratios, trace element systematics with close plume affinity and mantle-like Hf–O isotopic compositions demonstrate that these zircon cores were crystallized from mantle-derived magma at ~3.45 Ga (Fig. 2 and Supplementary Fig. 4). Even though the Longwan ultramafic–mafic rocks experienced high-pressure granulite-facies metamorphism at the end of the Neoproterozoic, most of their trace elements (for example, REEs and high field strength elements) were relatively immobile during the Neoproterozoic orogenic events, because these elements have positive linear correlations with Zr (Supplementary Fig. 8). The high Cr and Ni concentrations of meta-basalts argue that their elevated MgO contents are of original magmatic significance without metamorphic modification.

The meta-websterites are unlike any ultramafic–mafic lavas (for example, komatiites, picrites and boninites), but similar to experimental and natural pyroxenite cumulates^{16,17} (Fig. 3b), which suggests that they were crystallized from MgO-rich melts. The meta-lherzolites are also of cumulate origin, evidenced by their identical trace element patterns to meta-websterites (Fig. 3d). The correlation of Ni and V against Cr of the meta-basalts (Supplementary Fig. 9) implies that their protolith magmas experienced clinopyroxene-dominated (with olivine) fractionation. In addition, the meta-cumululates and the meta-basalts show complementary trends on Harker diagrams (Supplementary Fig. 5) and have almost indistinguishable ratios of Nb/Ta, Zr/Hf and Tb/Dy (Supplementary Fig. 10). Thus, it is highly likely that the meta-cumululates were crystallized from the same magmas parental to the meta-basalts when ascending and cooling to shallower magma chambers. Using bulk-rock Mg# of the meta-cumululates and Fe–Mg exchange coefficients, we calculated Mg# and liquidus temperatures of the melts that crystallized cumulus minerals (Methods). The results show that protoliths of the meta-cumululates were crystallized from relatively evolved melts with a Mg# of 62.2–67.8 at a temperature of ~1,200 °C (Supplementary Table 5). As for their crystallizing pressures, the lack of garnet in the meta-cumululates and their low Al_2O_3 content point to a shallow depth at

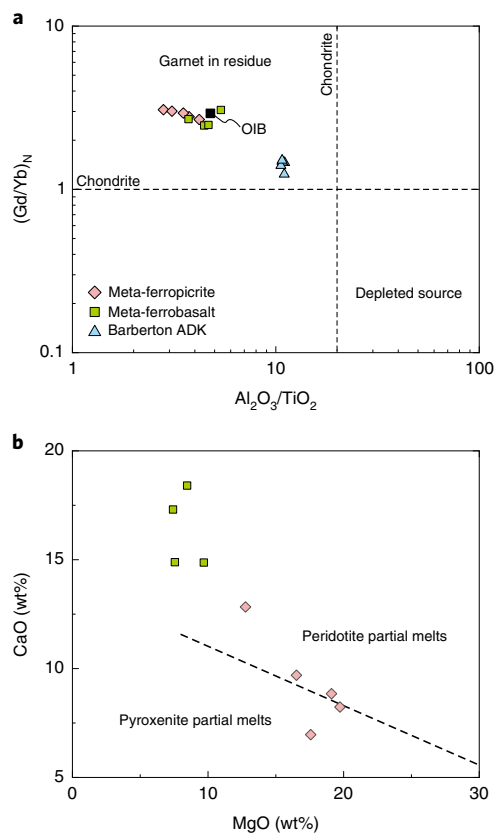


Fig. 4 | Geochemical diagrams for the meta-basalts of the Palaeoarchaean Longwan ultramafic-mafic suite. a, $\text{Al}_2\text{O}_3/\text{TiO}_2$ – $(\text{Gd}/\text{Yb})_N$ diagram⁴¹.

Chondrite and OIB values are from Sun and McDonough⁴⁰, the Barberton aluminium-depleted komatiites³ (ADKs) are also plotted for comparison and the meta-basalts of the Palaeoarchaean Longwan ultramafic-mafic suite have higher $(\text{Gd}/\text{Yb})_N$ and lower $\text{Al}_2\text{O}_3/\text{TiO}_2$ ratios than the Barberton ADKs. **b**, MgO – CaO diagram after Herzberg and Asimow¹⁹; the dashed line is the boundary to differentiate between peridotite-sourced melts (above the line) and pyroxenite-sourced melts (below the line). The major element oxides are recalculated on an anhydrous basis.

least below the garnet stability field, that is, spinel/plagioclase stability fields (~1–2 GPa).

The elevated iron contents of the meta-ferropicrites are distinguishable from typical picrites/komatiites but similar to iron-rich ferropicrites/ferrokamatiites (Fig. 3c). The meta-ferrobasalts ($\text{MgO} < 12 \text{ wt}\%$) have similar elevated iron contents and trace element characteristics to those of the meta-ferropicrites (Fig. 3). The meta-basalts are all enriched in compatible elements (Cr, Co and Ni), which suggests a derivation from a relatively high-degree melting of the mantle source. They are also enriched in Nb, Ta, Ti and LREEs, and their trace element patterns are similar to those of present-day OIB, indicative of an enriched mantle source (Fig. 3d). The uniformly high $(\text{Gd}/\text{Yb})_N$ (N, chondrite normalized), low $\text{Al}_2\text{O}_3/\text{TiO}_2$ ratios and Zr/Hf depletion (Figs. 3d and 4a) indicate the presence of residual garnet in their mantle source as garnet prefers to hold Zr, Hf, HREEs and Al_2O_3 at high pressures¹⁸. Their MgO – CaO systematics show that they were primarily derived from peridotite sources with minor contribution from pyroxenite¹⁹ (Fig. 4b). Therefore, the meta-ferropicrites have a close affinity with primary magmas, whereas the meta-ferrobasalts with lower MgO and Mg# could represent evolved melts from those of the meta-ferropicrites after the fractionation of clinopyroxene and olivine (Supplementary Fig. 9).

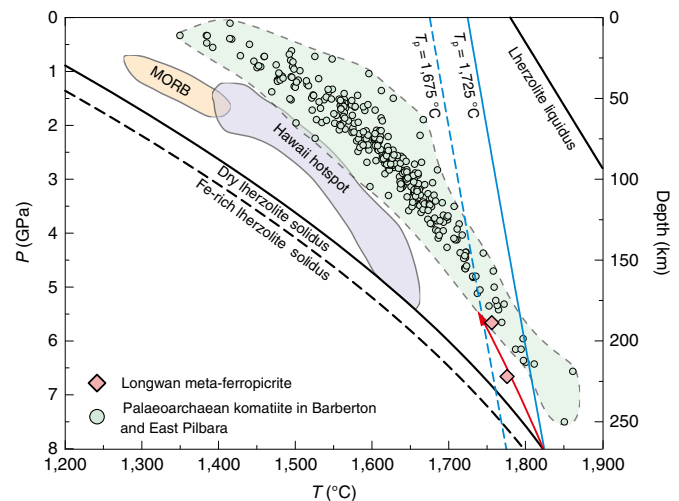


Fig. 5 | Calculated melting conditions for primary magmas of the meta-ferropicrites of the Palaeoarchaean Longwan ultramafic-mafic suite.

Melting conditions for the primary magmas of the most primitive meta-ferropicrite samples with the highest MgO contents (15LW-13 and 17LW-08) were calculated using thermobarometers based on the magma Si and Mg contents²⁰. T_p values were estimated by back calculating the melting conditions of the primary magmas along an isentropic melting adiabat until the melting adiabat intersected the solidus and then extrapolating from this intersection point along a solid mantle adiabat to the surface. The dry lherzolite solidus and liquidus are from Katz et al.⁴². The Fe-rich lherzolite solidus (heavy dashed line) was estimated by lowering the dry lherzolite solidus by $\sim 50^\circ\text{C}$ (ref. ²¹). Blue near-vertical lines represent the solid mantle adiabats with varying T_p ; the red curved line with an arrow corresponds to the isentropic melting adiabat; the melting conditions for MORB, Hawaii hotspot basalt and Palaeoarchaean komatiite are from Lee et al.²⁰.

We use FractionatePT software²⁰ to calculate the melting conditions for primary magmas of the most primitive meta-ferropicrite samples and the results indicate that their primary magmas were derived from the melting of mantle lherzolite at high pressures and temperatures (Fig. 5 and Supplementary Table 6), which corresponds to a mantle potential temperature (T_p) of $1,725^\circ\text{C}$. However, experimental studies have demonstrated that iron-rich lherzolites have systematically lower solidus temperatures than fertile peridotites by $\sim 50^\circ\text{C}$ (ref. ²¹), and thus the T_p for the meta-ferropicrites should be conservatively corrected to be $1,675^\circ\text{C}$. The melting conditions and T_p are comparable to those for Palaeoarchaean komatiites in Barberton and East Pilbara (Fig. 5). The above lines of evidence clearly point to a derivation of primary magmas of the meta-basalts through the melting of an anomalously hot mantle source at high pressures.

The estimated T_p for the Longwan meta-ferropicrites is $1,675^\circ\text{C}$, which implies that their mantle source was considerably hotter than the ambient mantle with a T_p of $1,500$ – $1,600^\circ\text{C}$ at 3.45 Ga (ref. ⁵). Such conditions, when ascending mantle material is significantly hotter than the surrounding mantle, are consistent with the mantle plume model^{22,23}. Their melting pressures should be comparable to or higher than those of the Barberton aluminium-depleted komatiites (Fig. 4a). Besides, the high Ni content of the Longwan meta-basalts argue for a strong affinity to mantle-plume-related rocks than that of their lower-temperature counterparts⁴. Ferropicrites are rare throughout geological history, and most Phanerozoic ferropicrite examples were identified at or near the base of volcanic sequences in continental large igneous province or continental flood basalt province settings, with a few cases in accreted oceanic plateaux^{24,25}. It is generally acknowledged that

large igneous provinces result from the arrival of a mantle plume head at the base of the lithosphere^{26–28}. Thus, it is most likely that the Longwan ultramafic–mafic suite represents remnants of volcanic successions generated during a Palaeoarchaeon (~3.45 Ga) mantle plume activity, dismembered during later intracrustal plutonic and tectonothermal activity.

Palaeoarchaeon deep mantle heterogeneity

Mantle plume activities were infrequent through the Archaean compared with the Proterozoic and the Phanerozoic²⁹. Komatiites and komatiitic basalts were generated by adiabatic decompression melting of upwelling mantle plumes at high mantle potential temperatures and pressures, and serve as records of mantle plume activities^{3,5}. The 3.45-Gyr-old Longwan ultramafic–mafic suite and the 3.5–3.46-Gyr-old komatiites in Barberton and East Pilbara are the oldest confirmed records of mantle plume activities^{1,2}. These Palaeoarchaeon mantle-plume-related rocks record the oldest recognized plume event in Earth's history and a counterpart to younger occurrences of global mantle plume activities³⁰. This global mantle plume event may indicate that large-scale deep mantle convection has been operating since the Palaeoarchaeon.

Partial melting of a typical peridotitic mantle alone cannot explain the iron-rich features observed in ferropicrites^{24,31–33}. It is commonly suggested that Archaean ferropicrites required an iron-rich peridotitic mantle source, although how to reach this iron enrichment remains controversial: the addition of recycled crustal material, an initially iron-rich mantle and subsequent iron sequestration, a core contribution and even an infall of iron-rich chondritic meteorites^{24,31–37}. Nonetheless, the occurrence of meta-ferropicrites and meta-ferrobasalts in the ~3.45-Gyr-old Longwan ultramafic–mafic suite indicates the existence of iron-rich domains in their Palaeoarchaeon deep mantle source. In addition, the enriched REE patterns and the relatively high melting degrees of these meta-ferropicrites and meta-ferrobasalts require an enriched deep mantle source, whereas the depleted and flat REE patterns of the 3.5–3.46-Gyr-old komatiites in Barberton and East Pilbara imply a depleted or primitive deep mantle source^{1,2,4} (Fig. 3d). Therefore, deep mantle heterogeneity was present in the Palaeoarchaeon, with a partial enrichment of iron and incompatible elements. Enriched domains in the Palaeoarchaeon deep mantle were most probably caused by the incorporation of recycled crustal material^{24,25,31}, and indicate an interaction between the lithosphere and mantle plumes, and the crustal recycling processes.

Online content

Any methods, additional references, Nature Research reporting summaries, source data, statements of code and data availability and associated accession codes are available at <https://doi.org/10.1038/s41561-019-0410-y>.

Received: 25 January 2019; Accepted: 14 June 2019;

Published online: 22 July 2019

References

- Arndt N. T., Leshner C. M., Barnes S. J. *Komatiite* (Cambridge Univ. Press, 2008).
- Barnes S. J., Arndt N. T. in *Earth's Oldest Rocks* 2nd edn (eds Van Kranendonk M. J., Bennett V. C. & Hoffmann J. E.) 103–132 (Elsevier, 2019).
- Sossi, P. A. et al. Petrogenesis and geochemistry of Archean komatiites. *J. Petrol.* **57**, 147–184 (2016).
- Campbell, I. & Griffiths, R. The changing nature of mantle hotspots through time: implications for the chemical evolution of the mantle. *J. Geol.* **100**, 497–523 (1992).
- Herzberg, C., Condie, K. & Korenaga, J. Thermal history of the Earth and its petrological expression. *Earth Planet. Sci. Lett.* **292**, 79–88 (2010).
- Nisbet, E. G., Cheadle, M. J., Arndt, N. T. & Bickle, M. J. Constraining the potential temperature of the Archaean mantle: a review of the evidence from komatiites. *Lithos* **30**, 291–307 (1993).
- Collerson, K. D., Campbell, L. M., Weaver, B. L. & Palacz, Z. A. Evidence for extreme mantle fractionation in early Archaean ultramafic rocks from northern Labrador. *Nature* **349**, 209–214 (1991).
- Polat, A., Hofmann, A. W. & Rosing, M. T. Boninite-like volcanic rocks in the 3.7–3.8 Ga Isua greenstone belt, West Greenland: geochemical evidence for intra-oceanic subduction zone processes in the early Earth. *Chem. Geol.* **184**, 231–254 (2002).
- Friend, C. R. L. & Nutman, A. P. Dunites from Isua, Greenland: a ca. 3720 Ma window into subcrustal metasomatism of depleted mantle. *Geology* **39**, 663–666 (2011).
- Liu, D. Y., Nutman, A. P., Compston, W., Wu, J. S. & Shen, Q. H. Remnants of ≥3800 Ma crust in the Chinese part of the Sino-Korean craton. *Geology* **20**, 339–342 (1992).
- Nutman, A. P. et al. Multistage late Neoproterozoic crustal evolution of the North China Craton, eastern Hebei. *Precambrian Res.* **189**, 43–65 (2011).
- Zhai, M.-G., Santosh, M. & Zhang, L. Precambrian geology and tectonic evolution of the North China Craton. *Gondwana Res.* **20**, 1–5 (2011).
- Wang, C., Song, S., Niu, Y., Wei, C. & Su, L. TTG and potassic granitoids in the eastern North China Craton: making Neoproterozoic upper continental crust during micro-continental collision and post-collisional extension. *J. Petrol.* **57**, 1775–1810 (2016).
- Corfu, F., Hancher, J. M., Hoskin, P. W. & Kinny, P. Atlas of zircon textures. *Rev. Mineral. Geochem.* **53**, 469–500 (2003).
- Kirkland, C. L., Smithies, R. H., Taylor, R. J. M., Evans, N. & McDonald, B. Zircon Th/U ratios in magmatic environs. *Lithos* **212–215**, 397–414 (2015).
- Müntener, O., Kelemen, P. B. & Grove, T. L. The role of H₂O during crystallization of primitive arc magmas under uppermost mantle conditions and genesis of igneous pyroxenites: an experimental study. *Contributions to Mineralogy and Petrology* **141**, 643–658 (2001).
- Lee, C.-T. A., Cheng, X. & Horodyskyj, U. The development and refinement of continental arcs by primary basaltic magmatism, garnet pyroxenite accumulation, basaltic recharge and delamination: insights from the Sierra Nevada, California. *Contrib. Mineral. Petrol.* **151**, 222–242 (2006).
- Corgne, A. et al. Trace element partitioning between majoritic garnet and silicate melt at 10–17 GPa: implications for deep mantle processes. *Lithos* **148**, 128–141 (2012).
- Herzberg, C. & Asimow, P. D. Petrology of some oceanic island basalts: PRIMELT2.XLS software for primary magma calculation. *Geochem. Geophys. Geosyst.* **9**, Q09001 (2008).
- Lee, C.-T. A., Luffi, P., Plank, T., Dalton, H. & Leeman, W. P. Constraints on the depths and temperatures of basaltic magma generation on Earth and other terrestrial planets using new thermobarometers for mafic magmas. *Earth Planet. Sci. Lett.* **279**, 20–33 (2009).
- Kushiro, I. in *Earth Processes: Reading the Isotopic Code* Vol. 95 (eds Basu, A. & Hart, S.) 109–122 (Wiley, 1996).
- Campbell, I. H., Griffiths, R. W. & Hill, R. I. Melting in an Archaean mantle plume: heads it's basalts, tails it's komatiites. *Nature* **339**, 697–699 (1989).
- Campbell, I. H. & Griffiths, R. W. Implications of mantle plume structure for the evolution of flood basalts. *Earth Planet. Sci. Lett.* **99**, 79–93 (1990).
- Gibson, S. A. Major element heterogeneity in Archean to Recent mantle plume starting-heads. *Earth Planet. Sci. Lett.* **195**, 59–74 (2002).
- Jennings, E. S., Holland, T. J. B., Shorttle, O., MacLennan, J. & Gibson, S. A. The composition of melts from a heterogeneous mantle and the origin of ferropicrite: application of a thermodynamic model. *J. Petrol.* **57**, 2289–2310 (2016).
- Coffin, M. F. & Eldholm, O. Large igneous provinces: crustal structure, dimensions, and external consequences. *Rev. Geophys.* **32**, 1–36 (1994).
- Saunders, A. D. Large igneous provinces: origin and environmental consequences. *Elements* **1**, 259–263 (2005).
- Ernst, R. E. & Jowitt, S. M. in *Tectonics, Metallogeny, and Discovery: the North American Cordillera and Similar Accretionary Settings* (eds Colpron, M., Bissig, T. et al.) 17–51 (Society of Economic Geologists, 2013).
- Ernst, R. & Bleeker, W. Large igneous provinces (LIPs), giant dyke swarms, and mantle plumes: significance for breakup events within Canada and adjacent regions from 2.5 Ga to the Present. *Can. J. Earth Sci.* **47**, 695–739 (2010).
- Barley, M. E., Krapez, B., Groves, D. I. & Kerrich, R. The Late Archaean bonanza: metallogenic and environmental consequences of the interaction between mantle plumes, lithospheric tectonics and global cyclicity. *Precambrian Res.* **91**, 65–90 (1998).
- Gibson, S. A., Thompson, R. N. & Dickinson, A. P. Ferropicrites: geochemical evidence for Fe-rich streaks in upwelling mantle plumes. *Earth Planet. Sci. Lett.* **174**, 355–374 (2000).
- Milidragovic, D. & Francis, D. Ca. 2.7 Ga ferropicritic magmatism: a record of Fe-rich heterogeneities during Neoproterozoic global mantle melting. *Geochim. Cosmochim. Acta* **185**, 44–63 (2016).

33. Zhang, J., Liu, Y., Ling, W. & Gao, S. Pressure-dependent compatibility of iron in garnet: insights into the origin of ferropicritic melt. *Geochim. Cosmochim. Acta* **197**, 356–377 (2017).
34. Hanski, E. J. & Smolkin, V. F. Iron- and LREE-enriched mantle source for early Proterozoic intraplate magmatism as exemplified by the Pechenga ferropicrites, Kola Peninsula, Russia. *Lithos* **34**, 107–125 (1995).
35. Stone, W. E., Crocket, J. H., Dickin, A. P. & Fleet, M. E. Origin of Archean ferropicrites: geochemical constraints from the Boston Creek Flow, Abitibi greenstone belt, Ontario, Canada. *Chem. Geol.* **121**, 51–71 (1995).
36. Francis, D., Ludden, J., Johnstone, R. & Davis, W. Picrite evidence for more Fe in Archean mantle reservoirs. *Earth Planet. Sci. Lett.* **167**, 197–213 (1999).
37. Goldstein, S. B. & Francis, D. The petrogenesis and mantle source of Archean ferropicrites from the Western Superior Province, Ontario, Canada. *J. Petrol.* **49**, 1729–1753 (2008).
38. Valley, J. W. Oxygen isotopes in zircon. *Rev. Mineral. Geochem.* **53**, 343–385 (2003).
39. Winchester, J. A. & Floyd, P. A. Geochemical discrimination of different magma series and their differentiation products using immobile elements. *Chem. Geol.* **20**, 325–343 (1977).
40. Sun, S. S. & McDonough, W. F. in *Magmatism in the Ocean Basins* (eds Saunders, A. D. & Norry, M. J.) 313–345 (Geological Society, 1989).
41. Arndt, N. Komatiites, kimberlites, and boninites. *J. Geophys. Res. Solid Earth* **108**(B6), 2293 (2003).
42. Katz, R. F., Spiegelman, M. & Langmuir, C. H. A new parameterization of hydrous mantle melting. *Geochim. Geophys. Geosyst.* **4**, 1073 (2003).

Acknowledgements

We thank S. Gibson for constructive discussions. This study was supported by the National Natural Science Foundation of China (grant nos 41430207, 41572040 and 41372060) and the Fundamental Research Funds for the Central Universities of China (grant no. 2652018115). C.Wang acknowledges the Chinese Scholarship Council for financial support during his visit to Durham University (grant no. 201606010063).

Author contributions

C.Wang and S.S. designed the project and wrote the manuscript. C.Wang, S.S., C.Wei and J.D. conducted fieldwork. C.Wang, L.S. and X.-H.L. performed all the analyses. All the authors contributed to the interpretation of the results and the revision of the manuscript.

Competing interests

The authors declare no competing interests.

Additional information

Supplementary information is available for this paper at <https://doi.org/10.1038/s41561-019-0410-y>.

Reprints and permissions information is available at www.nature.com/reprints.

Correspondence and requests for materials should be addressed to C.Wang or S.S.

Publisher's note: Springer Nature remains neutral with regard to jurisdictional claims in published maps and institutional affiliations.

© The Author(s), under exclusive licence to Springer Nature Limited 2019

Methods

In situ zircon U–Pb dating. Zircon grains were extracted from crushed samples by standard heavy-liquid and magnetic techniques, and purified by hand-picking under a binocular microscope. The selected grains were mounted in epoxy resin and polished down to about half-sections to expose the grain interiors, and then imaged under reflected and transmitted lights and by using CL. The CL images were acquired using a Panchromatic CL detector installed on a MIRA3 scanning electron microscope at the MOE Key Laboratory of Orogenic Belts and Crustal Evolution, Peking University. The mineral inclusions in zircons were identified using an Oxford INCA-Synergy energy dispersive spectroscopy installed on a FEI FEG 650 scanning electron microscope at Peking University.

Measurements of zircon U, Th and Pb isotopes were conducted using the CAMECA IMS-1280 SIMS at the Institute of Geology and Geophysics, Chinese Academy of Sciences, following the standard procedures described in Li et al.⁴³. The primary O²⁻ ion beam spot was about 20 × 30 μm in size. Analyses of the standard zircon Plešovice were interspersed with unknown grains. Pb/U calibration was performed relative to the zircon standard Plešovice⁴⁴; U and Th concentrations were calibrated against zircon standard 91500⁴⁵. To monitor the external uncertainties of SIMS zircon U–Pb dating calibrated against the Plešovice standard, an in-house zircon standard Qinghu was alternately analysed as an unknown together with other unknown zircons. A concordia age of 159.9 ± 1.2 Ma, which is identical within error to the recommended value of 159.5 ± 0.2 Ma (ref. 46), was yielded by 15 measurements on the Qinghu zircon. A long-term uncertainty of 1.5% (one relative s.d.) for ²⁰⁶Pb/²³⁸U measurements of the standard zircons was propagated to the unknowns. The measured compositions were corrected for common Pb using non-radiogenic ²⁰⁴Pb. Corrections were sufficiently small to be insensitive to the choice of common Pb composition, and an average of present-day crustal composition⁴⁷ was used for the common Pb assuming that the common Pb was largely surface contamination introduced during sample preparation. Data reduction was carried out using the Isoplot/Ex version 3.0⁴⁸. Uncertainties of individual analyses in the data tables are reported at the 1σ level.

In situ zircon oxygen isotope analyses. After the U–Pb dating, the sample mount was reground and repolished to ensure that any oxygen implanted in the zircon surface from the O²⁻ beam used for U–Pb dating was removed. Zircon oxygen isotopes were measured using the CAMECA IMS-1280 SIMS at the Institute of Geology and Geophysics, Chinese Academy of Sciences following standard procedures⁴⁹. The primary Cs⁺ ion beam spot was 10 μm in size. Oxygen isotopes were measured using the multicollection mode on two off-axis Faraday cups. The instrumental mass fractionation factor was corrected using the zircon standard 91500 with a δ¹⁸O/¹⁶O (ref. 50). The measured ¹⁸O/¹⁶O ratios were normalized using the Vienna Standard Mean Ocean Water compositions (¹⁸O/¹⁶O = 0.0020052) and reported in standard per million notation. A second zircon standard Qinghu was also analysed as an unknown to ascertain the veracity of the instrumental mass fractionation factor. Uncertainties on individual analyses are reported at the 1σ level. The internal precision of a single analysis was generally better than 0.2‰ (2σ) for the ¹⁸O/¹⁶O ratio. The external reproducibility of the ¹⁸O/¹⁶O ratios by repeated measurements of the standard zircon was better than 0.40‰. A weighted mean of δ¹⁸O = 5.38 ± 0.12‰ (2σ, n = 24) was yielded by 24 measurements of the Qinghu zircon standard during the course of this study, which is consistent, within errors, with the reported value of 5.4 ± 0.2‰ (ref. 46).

In situ zircon Hf isotope analyses. In situ zircon Hf isotope analyses of the dated sample were carried out using a Neptune multicollector inductively coupled plasma mass spectrometry attached with a New Wave UP-213 laser-ablation system (ICPMS) at the MLR Key Laboratory of Metallogeny and Mineral Assessment, Institute of Mineral Resources, Chinese Academy of Geological Sciences. The analytical details are given in Wu et al.⁵¹. A laser spot size of 40 μm was adopted for the analyses and helium gas was used as the carrier gas to transport the laser ablated sample from the laser-ablation cell to the ICPMS torch via a mixing chamber and mixed with argon gas. Correction for the isobaric interferences of ¹⁷⁶Lu and ¹⁷⁶Yb on ¹⁷⁶Hf was made following Wu et al.⁵¹. Before the analyses, standard zircons (TEMORA, GJ1 and FM02) were analysed and the efficacy of the correction method of isobaric interferences⁵¹ was tested. Zircon GJ1 was used as the reference standard to monitor data quality during the analyses, and gave a weighted mean ¹⁷⁶Hf/¹⁷⁷Hf ratio of 0.282015 ± 9 (2σ, n = 9), which is in accordance with the weighted mean ¹⁷⁶Hf/¹⁷⁷Hf ratio of 0.282000 ± 5 (2σ) measured by the solution analysis method⁵².

In situ zircon trace element analyses. Measurement of the trace elements in zircons were carried out on an Agilent-7500a quadrupole ICPMS coupled with a New Wave UP-193 solid-state laser-ablation system in the Geological Lab Center, China University of Geosciences. A laser spot size of 36 μm, laser energy density of 8.5 J cm⁻² and a repetition rate of 10 Hz were used for the analyses. The ablated sample material was carried into the ICPMS system by high-purity helium gas. Calibrations for the element concentrations were carried out using NIST 610 glass and Harvard standard zircon 91500 as the external standards, with recommended values taken from Wiedenbeck et al.⁴⁵ and Pearce et al.⁵³ and using ²⁹Si as an internal standard. NIST 612 and 614 glasses served as the monitoring standards

simultaneously. The analytical accuracy for trace elements in the zircons was better than ±10% with abundances >10 ppm and ±15% with abundances <10 ppm.

Bulk-rock major and trace element analyses. All the samples were fresh cuttings away from late veinlets, any surface contaminants were trimmed off and the cuttings were then thoroughly cleaned. Fresh portions of the trimmed samples were crushed into 1–2 cm size chips using a percussion mill. These rock fragments were ultrasonically cleaned in Milli-Q water, dried and powdered in a thoroughly cleaned agate mill to 200 mesh in the clean laboratory at the Langfang Regional Geological Survey. Bulk-rock major and trace element analyses were done in the Geological Lab Center, China University of Geosciences following the procedures described in Song et al.⁵⁴. Major elements were analysed on a Leeman Prodigy inductively coupled plasma–optical emission spectroscopy system with high dispersion Echelle optics. Based on rock standards AGV-2, W-2 (US Geological Survey), GSR-1 and GSR-3 (national geological standard reference materials of China), the analytical precisions (1σ) for most major element oxides were better than 1% with the exception of TiO₂ (~1.5%) and P₂O₅ (~2.0%). Loss on ignition was determined by placing 1 g of samples in a furnace at 1,000 °C for a few hours and then reweighing the cooled samples.

Bulk-rock trace elements were analysed using an Agilent-7500a quadrupole ICPMS. About 35 mg of powder of each sample was dissolved in a distilled acid mixture (1:1 HF:HNO₃) with Teflon digesting vessels and heated on a hotplate at 195 °C for 48 h using high-pressure bombs for digestion and/or dissolution. The sample was then evaporated to incipient dryness, refluxed with 1 ml of 6N HNO₃ and heated again to incipient dryness. The sample was again dissolved in 2 ml of 3N HNO₃ and heated at 165 °C for a further 24 h to guarantee complete digestion and/or dissolution. The sample was finally diluted with Milli-Q water to a dilution factor of 2,000 in a 2% HNO₃ solution for the ICPMS analyses. Rock standards AGV-2, W-2 and BHVO-2 (US Geological Survey) were used to monitor the analytical accuracy and precision. Analytical accuracy, as indicated by relative difference between measured and recommended values, was better than 5% for most elements, and about 10–15% for Cu, Zn, Gd and Ta.

Calculation of Mg# and liquidus temperatures for melts in equilibrium with meta-cumulates. Cumulus minerals should be in equilibrium with the melts from which they precipitated and the liquidus temperature of basaltic melts is proportional to the MgO contents in the melts^{55–57}. Thus, the Mg# and liquidus temperatures of the melts that crystallize cumulus minerals can be calculated using the well-established Fe–Mg exchange coefficients ($K_D(\text{Fe–Mg})^{\text{mineral-liquid}} = (\text{Mg}^{\text{liquid}}/\text{Fe}^{2+\text{liquid}})/(\text{Mg}^{\text{mineral}}/\text{Fe}^{2+\text{mineral}})$). As the meta-cumulates experienced high-pressure granulite-facies metamorphism at the end of the Archaean and Fe–Mg re-exchanges should have occurred between minerals during this high-grade metamorphism, the compositions of the pyroxenes or olivines present in the meta-cumulates cannot represent primitive compositions in the equilibrium with the melts. However, $K_D(\text{Fe–Mg})^{\text{opx-liquid}}$ (0.28 ± 0.08) is similar to $K_D(\text{Fe–Mg})^{\text{opx-liquid}}$ (0.29 ± 0.06) and $K_D(\text{Fe–Mg})^{\text{ol-liquid}}$ (0.30 ± 0.03) (cpx, clinopyroxenes; opx, orthopyroxenes; ol, olivine)^{58,59}, which allows us to use the bulk-rock Mg# of the meta-cumulates to estimate the nature of their parental magma. The effect of trapped liquid crystallization on the cumulus mineral compositions⁶⁰ means that the calculated Mg# and liquidus temperatures should represent minimum estimates for the equilibrated melts. The equations are:

$$\text{Mg\#}(\text{equilibrated melts}) = 1 / \{ [1 / \text{Mg\#}(\text{bulk} - \text{rock}) - 1] / K_D(\text{Fe} - \text{Mg}) + 1 \} \quad (1)$$

where $K_D(\text{Fe–Mg}) = 0.28$ for meta-websterites and 0.30 for meta-lherzolites;

$$T_{\text{liquidus}}(\text{ }^\circ\text{C}) = 1,066 + 12.067\text{Mg\#} + 312.3(\text{Mg\#})^2; \quad (2)$$

$$\text{Mg\#} = \text{molar Mg} / (\text{Mg} + \text{Fe}). \quad (3)$$

Data availability

The authors declare that all data supporting the findings of this study are available within the article and its Supplementary Information files.

References

- Li, X.-H., Liu, Y., Li, Q.-L., Guo, C.-H. & Chamberlain, K. R. Precise determination of Phanerozoic zircon Pb/Pb age by multicollector SIMS without external standardization. *Geochem. Geophys. Geosyst.* **10**, Q04010 (2009).
- Sláma, J. et al. Plešovice zircon—a new natural reference material for U–Pb and Hf isotopic microanalysis. *Chem. Geol.* **249**, 1–35 (2008).
- Wiedenbeck, M. et al. Three natural zircon standards for U–Th–Pb, Lu–Hf, trace element and REE analyses. *Geostandard. Newslett.* **19**, 1–23 (1995).
- Li, X.-H. et al. Qinghu zircon: a working reference for microbeam analysis of U–Pb age and Hf and O isotopes. *Chinese Sc. Bull.* **58**, 4647–4654 (2013).

47. Stacey, J. S. & Kramers, J. Approximation of terrestrial lead isotope evolution by a two-stage model. *Earth Planet. Sci. Lett.* **26**, 207–221 (1975).
48. Ludwig K. R. *User's Manual for Isoplot 3.0: A geochronological toolkit for Microsoft Excel* (Berkeley Geochronology Centre, 2003).
49. Li, X.-H. et al. Petrogenesis and tectonic significance of the ~850 Ma Gangbian alkaline complex in South China: evidence from in situ zircon U–Pb dating, Hf–O isotopes and whole-rock geochemistry. *Lithos* **114**, 1–15 (2010).
50. Wiedenbeck, M. et al. Further characterisation of the 91500 zircon crystal. *Geostandard. Geoanal. Res.* **28**, 9–39 (2004).
51. Wu, F.-Y., Yang, Y.-H., Xie, L.-W., Yang, J.-H. & Xu, P. Hf isotopic compositions of the standard zircons and baddeleyites used in U–Pb geochronology. *Chem. Geol.* **234**, 105–126 (2006).
52. Morel, M. L. A., Nebel, O., Nebel-Jacobsen, Y. J., Miller, J. S. & Vroon, P. Z. Hafnium isotope characterization of the GJ-1 zircon reference material by solution and laser-ablation MC-ICPMS. *Chem. Geol.* **255**, 231–235 (2008).
53. Pearce, N. J. G. et al. A compilation of new and published major and trace element data for NIST SRM 610 and NIST SRM 612 glass reference materials. *Geostandard. Newslett.* **21**, 115–144 (1997).
54. Song, S. G. et al. Tracing the 850-Ma continental flood basalts from a piece of subducted continental crust in the North Qaidam UHPM belt, NW China. *Precambrian Res.* **183**, 805–816 (2010).
55. Weaver, S. J. & Langmuir, C. H. Calculation of phase equilibrium in mineral-melt systems. *Comput. Geosci.* **16**, 1–19 (1990).
56. Niu, Y. Mantle melting and melt extraction processes beneath ocean ridges: evidence from abyssal peridotites. *J. Petrol.* **38**, 1047–1074 (1997).
57. Niu Y., Gilmore T., Mackie S., Greig A., Bach W. Mineral chemistry, whole-rock compositions, and petrogenesis of Leg 176 gabbros: data and discussion. In *Proc. Ocean Drilling Program, Scientific Results Vol. 176* (eds Natland, J. H., Dick H. J. B. et al.) 1–60 (Ocean Drilling Program, 2002).
58. Roeder, P. L. & Emslie, R. F. Olivine-liquid equilibrium. *Contrib. Mineral. Petrol.* **29**, 275–289 (1970).
59. Putirka, K. D. Thermometers and barometers for volcanic systems. *Rev. Mineral. Geochem.* **69**, 61–120 (2008).
60. Barnes, S. J. The effect of trapped liquid crystallization on cumulus mineral compositions in layered intrusions. *Contrib. Mineral. Petrol.* **93**, 524–531 (1986).